Journal of Materials Chemistry A

Local Structure and Ions Storage Properties of Vanadate Cathode Materials Regulated by the Pre-Alkalization

Journal:	*Journal of Materials Chemistry A*
Manuscript ID	TA-ART-06-2022-004490.R1
Article Type:	Paper
Date Submitted by the Author:	07-Aug-2022
Complete List of Authors:	Teng, Xiaowei; University of New Hampshire, Chemical Engineering; Worcester Polytechnic Institute, Chemical Engineering Shan, Xiaoqiang; University of New Hampshire, Chemical Engineering Kim, SaeWon; University of New Hampshire, Chemical Engineering Abeykoon, Milinda; Brookhaven National Laboratory, Photon Science Division - National Synchrotron Light Source II Kwon, Gihan; Brookhaven National Laboratory, Photon Science Division - National Synchrotron Light Source II Olds, Daniel; Brookhaven National Laboratory, Photon Science Division - National Synchrotron Light Source II

ARTICLE

Local Structure and Ions Storage Properties of Vanadate Cathode Materials Regulated by the Pre-Alkalization

Received 00th January 20xx,
Accepted 00th January 20xx

DOI: 10.1039/x0xx00000x

Xiaoqiang Shan,[a,#] SaeWon Kim,[a,#] Milinda Abeykoon,[b] Gihan Kwon,[b] Daniel Olds,[b] and Xiaowei Teng*[a, c]

Aqueous Zn-ion batteries using mild acidic electrolytes utilizing a Zn^{2+}/H^+ dual-ion storage mechanism have shown great potential in achieving high energy density comparable to non-aqueous lithium-ion batteries. This study revealed that hydrated alkali-ions regulate the formation of alkali-intercalated vanadates layered compounds. Among various vanadate materials, lithium-intercalated vanadate has the largest interlayer spacing and most disordered local structure, exhibiting the largest storage capacity of 308 mAh g^{-1} at 0.05 A g^{-1} for Zn^{2+}/H^+ dual-ion storage and improved charge transfer and transport kinetics and cycling performance, evidenced by *in situ* X-ray diffraction and *ex situ* X-ray total scattering and pair distribution function analysis. Our study provides new insight into designing the layered vanadate materials for high-capacity aqueous batteries.

Introduction

Metal-ion batteries have become a key technology for a wide range of applications, including portable electronics and electric vehicles.[1, 2] Although lithium-ion batteries (LIBs) based on an intercalation charge storage mechanism are the dominant battery technology, their safety (e.g., toxic and flammable electrolytes), material and manufacturing costs associated with supply chain crunch (e.g., lithium, cobalt, and nickel raw materials) have been lingering concerns.[3] Aqueous rechargeable zinc ion battery (ARZIBs) utilizing Zn metal anode has attracted increasing attention for several reasons. Firstly, Zn metal has a high theoretical specific capacity of 820 mAh g^{-1}; Secondly, Zn^{2+}/Zn redox occurs at low potential (-0.76 V *vs.* SHE), providing a wide operation voltage window for ARZIB cells;[4-7] Thirdly, mildly acidic electrolytes, resulting from the usage of $ZnSO_4$ or $Zn(CF_3SO_3)_2$ salt, enable the Zn^{2+} and H^+ dual-ion storage in the cathodes for a much-enhanced storage capacity.[8-10] Advances in Zn-hosting cathode materials, such as layered transition metal oxides (TMOs, e.g., manganese and vanadium oxides),[8, 9, 11] transition metal polyanions,[12-14] conductive polymers or organic frameworks,[15, 16] and Prussian blue type cathodes,[17, 18] offered a large open-frameworks to facilitate a variety of battery chemistry involving Zn^{2+}/H^+ intercalation or conversion.

Among various layered TMOs, monoclinic vanadate $AV_3O_8{\cdot}nH_2O$ (A: intercalated ions) has been considered one of the most promising cathodes for ARZIBs due to its high theoretical capacity (343 mAh g^{-1}, based on the one-electron transfer reaction).[10, 19-22] Great efforts have been made to tailor the structure of the vanadate to significantly influence the storage capacity and kinetics of charge transfer and transport processes. For instance, enlarged V-O interlayer spacing and more structural water molecules between V-O layers help store more cations and promote Zn^{2+}/H^+ diffusion.[23-27] Notably, vanadate is made of negatively charged V-O bilayers, which comprise edge-sharing [VO_6] octahedra and [VO_5] pyramids and are stacked along the <001> direction. The positively charged proton, alkali, or alkaline earth metal ions are pre-intercalated in the interlayers, formed during the materials synthesis, and interact with negatively charged V-O polyhedral layers by *van der Waals* force.[25, 28] It was expectable that these intercalated cations don't actively participate in the insertion/extraction processes during the ARZIBs charging and discharging processes. Instead, they function as a structural pillar to stabilize the V-O layers and thus mitigate capacity degradation during the electrochemical cycling.[26] Given the important role of pre-interacted ions, contrastingly, their influences on vanadate's material chemistry and electrochemical properties have not been comprehensively studied.

Recently, a dissolution-recrystallization approach has been reported to prepare TMOs and metal borides electrode materials.[29-32] The method involves the treatment of TMOs and metal borides bulk raw materials with solutions of alkali and alkaline earth metal salt solution. The bulk raw materials, when subjected to dissolution and recrystallization in the aqueous solution in the presence of alkali metal salt, alkaline earth metal salt, or even conductive polymer,[33] tend to grow preferentially in lateral dimensions. The resulting nanostructured electrode materials showed a large open-framework and improved electrochemical properties in reversibly hosting monovalent

[a] *Department of Chemical Engineering, University of New Hampshire, Durham, New Hampshire 03824, USA*
[b] *National Synchrotron Light Source II, Brookhaven National Laboratory, Upton, New York 11973, USA*
[c] *Department of Chemical Engineering, Worcester Polytechnic Institue, Worcester, Massachusettes 01609, USA*
# authors made equal contributions to the publication
Electronic Supplementary Information (ESI) available: [details of any supplementary information available should be included here]. See DOI: 10.1039/x0xx00000x

and multivalent charge carriers for energy storage applications, including ARZIBs. However, this pre-alkalization approach was used mostly for pre-sodiation with a few examples of potassiation. It remained unclear whether it is applicable to tuning material characteristics for Zn^{2+}/H^+ storage by tailoring the alkali-TMOs interaction.

Here we report solution-based pre-alkalization of vanadate Zn-ion cathode materials with lithium, sodium, and potassium salts inorganic compounds (Li_2SO_4, Na_2SO_4, and K_2SO_4). We found that the hydrated alkali metal ions regulated the formation of $AV_3O_8{\cdot}nH_2O$. Different from the vanadate prepared from sodiation (NaVO) and potassiation (KVO) processes, synchrotron X-ray scattering analysis shows the pre-lithiation forms distinct lithium-ion-intercalated disordered vanadate (LiVO) with the larger interlayer spacing, more vacant sites, higher portion of [VO_5] pyramid building units (namely, less edge-sharing building blocks). The highly disordered LiVO exhibits improved Zn^{2+}/H^+ transport properties and thus superior electrochemical performance for ARZIBs with a high specific capacity of 308 mAh g^{-1} at 0.05 A g^{-1}, improved redox kinetics, and the capacity retention of 96% (0.4 A g^{-1} for 200 cycles) and 89% (1 A g^{-1} for 800 cycles), respectively. Our study provides a fundamental understanding of the roles of pre-intercalation alkali in optimizing the local structure of TMO electrodes that have advanced properties for ARZIBs, such as large capacities and excellent rate capabilities.

Experimental

Materials synthesis and characterizations For the preparation of LiVO materials, 100 mg commercial V_2O_5 powder (Sigma-Aldrich, Inc.) are dispersed in a 20 mL vial containing 9 mL Li_2SO_4 (Alfa Aesar, Inc.) with a concentration of 0.5 M and stirred for six days (144 hours). After that, the product is washed with deionized water and ethanol and then vacuum-dried overnight at room temperature. The NaVO and KVO products are obtained by a similar method, except a 0.5 M Na_2SO_4 or 0.5 M K_2SO_4 (Alfa Aesar, Inc.) and 300 mg V_2O_5 powder are used. The SEM images are collected using a Tescan Lyra3 GMU FIB scanning electron microscopy at the University of New Hampshire (UNH). A concentration of 0.5 M salt solution was chosen because of the solubility limit of K_2SO_4 in water.

Electrochemical measurements The inks are prepared with a mixture of 80% pre-alkalized vanadate materials (AVO, A: Li^+, Na^+, and K^+), 18% carbon black, and 2% styrene-butadiene rubber binders (SBR, MTI Inc.) which are deposited on the Toray carbon paper with a diameter of 18 mm (a geometric surface area about 2.54 cm^2). The loading of active materials on each electrode is about 2.4 mg cm^{-2}. The cellulose-based filter paper (Whatman Inc.) is used as the separators, and Zn foil (Alfa Aesar Inc.) with a diameter of 18 mm is used as the anode. The $ZnSO_4$ electrolyte (3M) is prepared, and 300 μL is loaded into the cell. These cell components, including vanadate cathodes, separator, electrolyte, and Zn anode, are assembled into an electrochemical cell (model: ECC-Aqu, El-Cell Inc.). The chronopotentiometry (CP) galvanostatic charge and discharge measurements are conducted in the assembled cells with a voltage range between 0.2 V and 1.4 V (*vs.* Zn^{2+}/Zn) at the current density of 0.05A g^{-1}, and detailed dQ/dV data analysis is also provided. The long-term cycling stability of AV_3O_8 is tested in the same voltage range (0.2 V - 1.4 V) at the current densities of 0.4 A g^{-1} (for 200 cycles) and 1 A g^{-1} (for 800 cycles). All the results from CP measurements and responding dQ/dV data analysis in two-electrode cells are presented after three formation cycles. The rate performance with CPs is tested at 0.05, 0.1, 0.2, 0.4, 0.8, 1, 2 and 5 A g^{-1} and returned to 0.2 A g^{-1} for 85 cycles. Cyclic voltammetry (CV) measurements are conducted in the assembled cells at the scan rates from 0.05 mV s^{-1} to 2 mV s^{-1} between 0.2 V and 1.4 V (vs. Zn^{2+}/Zn). Electrochemical Impedance Spectroscopy (EIS) measurements are conducted at the open circuit voltages of AVO electrodes with a perturbation of 5 mV and frequency ranging from 0.01 Hz to 100 kHz. Galvanostatic intermittent titration technique (GITT) measurements are conducted at the current density of 0.025 A g^{-1} for three discharge and charge segments between 0.2 V and 1.4 V (vs. Zn^{2+}/Zn). The discharge or charge time for each step is 10 minutes and then relaxed for another 10 minutes to reach the equilibrium state.

***In situ* XRD and X-ray PDF characterizations for zinc battery** *In-situ* X-ray scattering measurements, including X-ray diffraction (XRD) and pair distribution function (PDF) measurements, are conducted in a homemade electrochemical cell at the beamline 28-ID-1 at Brookhaven National Laboratory with the wavelength of 0.166 Å. The electrode material is deposited on thin carbon paper, dried naturally in the open air, and placed in the electrochemical cell as the cathode. Zn disk with a 5 mm hole (X-ray beam pass) is used as the counter and reference electrodes. $ZnSO_4$ electrolyte (3M, 300 μl) is loaded on the cellulose-based separators and stacked between the anode and cathode. CV scans were applied at a scan rate of 0.5 mV s^{-1} between 0.2 V and 1.4 V (vs. Zn^{2+}/Zn), and the X-ray scattering data were collected during cycling. XRD data are analyzed by using GSAS II software.

Results and discussion

Material synthesis and Local structures

Pre-lithiated vanadate (LiVO) is synthesized by stirring V_2O_5 bulk material in 0.5 M Li_2SO_4 at room temperature for six days. Synchrotron (XRD) analysis shows the structural evolution from orthorhombic V_2O_5 bulk to monoclinic layered LiVO during the material synthesis (**Figures 1a and S1**). Monoclinic LiVO has a P 21/m symmetry, sharing an isomorphic structure with $H_2V_3O_8$ (JCPDS-85-2401) and NaV_3O_8 (JCPDS-89-0621), as shown in **Figure S2a**. Compared to V_2O_5 bulk materials, the (001) peak of LiVO shifts to a smaller diffraction angle, suggesting a larger (001) interlayered spacing (d_{001}) of 11.3 Å. The increase in d_{001} is also accompanied by a high ratio of intercalated structural water (5.5%), as shown in thermogravimetric analysis (TGA) (**Figure S2b**).Their SEM images are shown in **Figure S2e-S2g**. In

addition to Rietveld refinement of XRD patterns that only analyzes the long-range order of materials, the aperiodic information that lies in local structure is obtained from X-ray total (diffuse and Bragg) scattering and PDF analysis. X-ray PDF fitting results are shown in **Figure 1b**, and detailed lattice parameters are provided in **Table S1**.

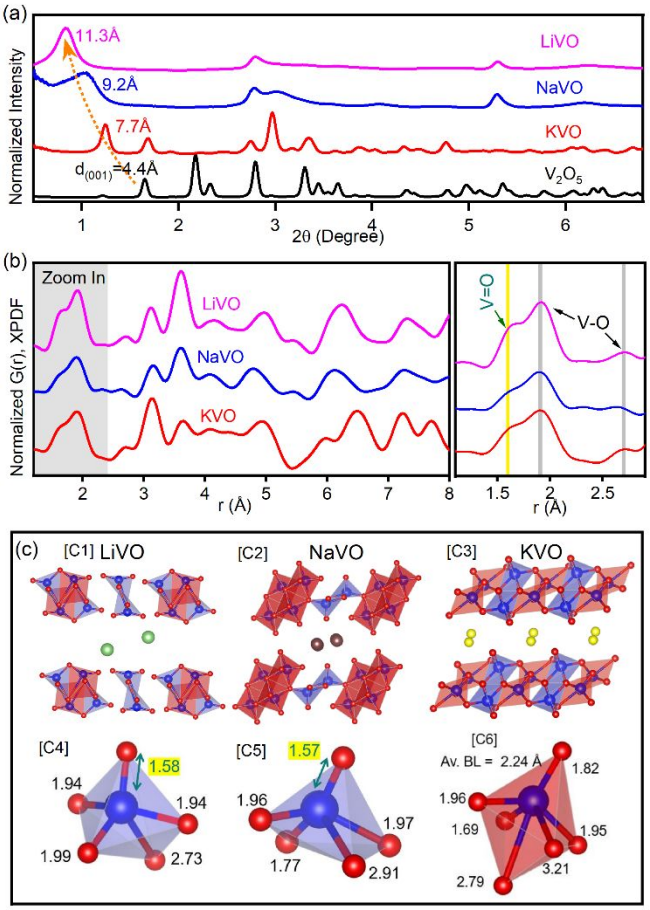

Figure 1. (a) XRD patterns with the phase evolution from V_2O_5 to AVO (A: Li, Na, K); (b) Fitted PDF patterns of AVO and the zoom-in showing V-O double and single bond lengths near 1.5 Å; (c) [c1-3] Crystal lattice structure of LiVO, NaVO, and KVO; LiVO's building block units: [c4, 5] VO_5 bipyramids structure and [c6] VO_6 octahedra with individual and averaged V-O bond lengths (VO_5 pyramid in blue and VO_6 octahedral in red, green: Li, blue: V, red: O).

The PDF analysis shows that LiVO is packed with V_3O_8 layers comprising VO_6 octahedra and VO_5 trigonal pyramids and held together by hydrated intercalated Li-ions (**Figure 1c**), in stark contrast to V_2O_5 bulk materials made up of continuously connected VO_5 pyramid units.

For NaVO and KVO, pre-sodiation and pre-potassiation were performed with solutions of Na_2SO_4 and K_2SO_4 at room temperature (**Figure S3**). Notably, NaVO and KVO vanadates require a much shorter reaction time than LiVO for a complete pre-alkalization process (V_2O_5 → AV_3O_8), following the order of LiVO > NaVO > KVO, opposite to the hydrated ionic radius sequence (**Figure S4**). Similar trends are also found in several structural characteristics, such as disorder, d_{001} value, and structural water ratio (**Table 1 and Tables S2-S3**).

Notably, three AV_3O_8 materials have similar long-range order, such as the same layered structure under the P21/m space group and the same types of VO_5/VO_6 building units (**Figures 1c** and **S5**), as suggested by XRD analysis. However, X-ray PDF analysis shows that three materials have different local structures. Specifically, the VO_5 pyramid has the unique V=O atomic pair with a short vanadyl bond length (~ 1.57 Å), the characteristic feature that cannot be found in the VO_6 octahedra. **Figure 1b** shows X-ray PDF results, where the relative intensity between the peaks at ~1.6 Å (V=O pair from VO_5 pyramid) and ~1.9 Å (V-O pairs from both VO_5 pyramids and VO_6 octahedra) is higher in LiVO than those in NaVO and KVO. These results suggest LiVO has a high portion of VO_5 pyramids connected via edge-sharing and more vacancy sites within the V-O framework (**Figure 1c**). On the contrary, NaVO and KVO are made up of VO_5 and VO_6 connected via edge- and corner-sharing, showing a more densely packed V-O framework in the *a-b* plane. The highly disordered nature of LiVO is also supported by its larger isotropic atomic displacement parameters (U_{iso}) value (0.11 $Å^2$) from Rietveld refinement of X-ray scattering than NaVO (0.06 $Å^2$) and KVO (0.01 $Å^2$). Notably, the U_{iso} value is closely related to the mean atomic displacements, e.g., U = $<u^2>$, where *u* is an instantaneous atomic displacement. A large U_{iso} value is a good representation of a disordered structure.

All these collective structural details suggest that hydrated alkali plays a critical role in the formation of AV_3O_8 vanadate (**Figure 2**). Among the three alkali ions studied here, Li-ion has the highest hydration enthalpy and the largest hydrated radius, bringing more water molecules coordinated in the hydrated shell during the pre-alkalization material synthesis process. Thus, the resulting LiVO has the most disordered local structure and the largest interlayer spacing, possibly due to more structural water molecules brought by the Li-ion and intercalated in the interlayer regions between the V-O frameworks. This hypothesis is supported by the following three control pre-alkalization experiments, conducted with (i) no salt additive, (ii) H_2SO_4, and (iii) $(NH_4)_2SO_4$. Specifically, when V_2O_5 bulk was stirred in water without any salt, XRD analysis found no vanadate formation (**Figure S6**); When V_2O_5 bulk was stirred in water with only H_2SO_4 (same concentration of alkali sulfate salts), XRD analysis also confirmed no vanadate phase occurred, either. These results suggested that hydronium (H_3O^+) cannot assist vanadate formation due to the inadequately hydrated water molecules it could bring to the pre-alkalization process. Interestingly, when V_2O_5 bulk stirred in water with $(NH_4)_2SO_4$

Table 1. Summary of AVO structural properties.

	LiVO	NaVO	KVO
Hydrated Radius of Alkali (Å)	3.82	3.58	3.31
Pre-alkalization reaction time (day)	6	3	1
Structural water molar ratio (%)	5.5	8.2	0.26
d_{001} (Å)	11.3	9.2	7.7
U_{iso} ($Å^2$)	0.11	0.06	0.01
Discharge capacity ($mAhg^{-1}$, 1st cycle, 0.05 Ag^{-1})	308	265	70
Capacity retention (%, 200th cycle, 0.4 A g^{-1})	96	85	87
b-value	0.88	0.64	0.64

salt, the vanadate phase formed with nearly identical structural characteristics to KVO. This result agrees well with our hypothesis that the hydration of alkali-ions plays a critical role in forming vanadate materials during the pre-alkalization process because the ionic radius and hydration number of NH_4^+ and K^+ are very similar (**Table S4**). It is also worth mentioning that the hydration property of alkali metal ions not only determines the local structure of the AV_3O_8 vanadate by

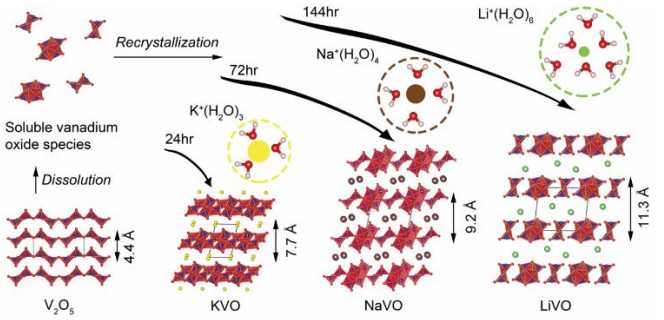

Figure 2. Hydrated alkali metal-ions (A: Li, Na, K) regulate crystal structure formation of AVO vanadate with reaction rates and kinetics after the process of dissolution of V_2O_5 bulk precursors and recrystallization (for atoms in the crystal structure, V: blue, O: red, Li: green, Na: brown, K: yellow, H^+ and H_2O are neglected considering residing at the same site of alkali metal-ions).

regulating the structural water in the V-O framework, but also takes its toll on the pre-alkalization kinetics. As shown in **Table 1**, LiVO formation requires the longest reaction time for the complete conversion from V_2O_5 to LiV_3O_8 (six days). This sluggish pre-alkalization kinetics is due to the lowest ionic mobility of Li-ions (33.5 ohm^{-1} cm^2 mol^{-1}) compared to Na- and K-ions (**Table S4**). Notably, the formation of AV_3O_8 materials is governed by the complete reaction between alkali salt solution and V_2O_5 powder. Therefore, the stoichiometric ratio of alkali cation in AV_3O_8 likely reached an equilibrium. However, the electrochemical charge or discharge of AV_3O_8 materials in alkali salt solution could provide means to further modify the stoichiometric ratio of alkali cation and will be explored in future studies.

Electrochemical performance of AV_3O_8 in Zn-ion batteries

Electrochemical properties of AV_3O_8 vanadates as the cathode materials for ARZIBs were evaluated in a two-electrode cell using a 3 M $ZnSO_4$ electrolyte and a zinc disk functioning both as the reference and counter electrodes. **Figure 3a** shows chronopotentiometry (CP) results at the current density of 0.05 A g^{-1} in the voltage window between 0.2 V and 1.4 V (*vs.* Zn^{2+}/Zn), and corresponding differential capacity curves (dQ/dV *vs.* V) are plotted in **Figure 3b**. Three vanadate materials demonstrated very reversible redox processes, showing two charging plateaus (~ 0.75 V and ~ 1.0 V) and discharging plateaus (~ 0.57 V and ~ 0.87 V), whereas LiVO shows the largest 1st cycle discharge capacity (308 mAh g^{-1}), relative to NaVO (265 mAh g^{-1}) and KVO (70 mAh g^{-1}). Rate performance and the long-term cycling performance of three vanadate materials are shown in **Figure 3c**, where LiVO demonstrated the most superior performance. As current density increased from 0.05 to 5 A g^{-1}, LiVO showed capacity values ranging from 308 mAh g^{-1} (0.05 A g^{-1}) to 33 mAh g^{-1} (5 A g^{-1}). And as the current density returns to 0.2 A g^{-1}, the capacity of LiVO remained 200 mAh g^{-1}, showing little capacity loss. The long-term cycling performance of the three materials is shown in **Figure 3d**. Again, LiVO has an excellent cycling performance with capacity retention of 96% at 0.4 A g^{-1} after 200 cycles, much better than those of NaVO (85%) and KVO (87%). At a higher current density (1 A g^{-1}) and longer cycling (800 cycles), LiVO remained a high value of capacity retention (89%, **Figure S7**).

Besides superior storage capacity, rate performance, and cycle life, LiVO also shows great kinetics during the charge transfer and transport processes. We first analyzed the rate-dependent reaction kinetics of the charge storage process of three vanadate materials. Basically, we conduct the cyclic voltammetry (CV) with scan rates ranging from 0.05 mV s^{-1} to

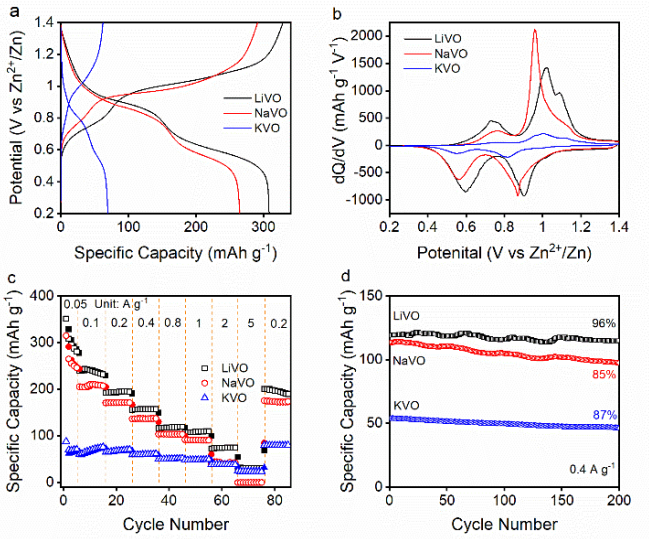

Figure 3. (a) CPs of AVO at the current density of 0.05 A g^{-1} in an aqueous zinc-ion battery (1st cycle data); (b) Differential capacity curves of AVO obtained from (a); (c) Rate performance of AVO up to 85 cycles; (d) Cycling stability of AVO at 0.4 A g^{-1} for 200 cycles.

2 mV s^{-1} (**Figures 4a** and **S8**). Assuming peak current (i) in CVs obeys a power relationship with respect to the scan rate (v) as the Equation 1 shows:[34, 35]

$$I = av^b \qquad \text{Equation 1}$$

where *a* and *b* are constants. Traditionally, a *b*-value of 0.5 suggested a slow charge transfer process, often observed in a diffusion-limited redox process. On the other hand, a *b*-value of 1.0 suggests a quick charge transfer, often a characteristic of a surface-controlled capacitive process. **Figure 4b** shows the *b*-values of three AVOs calculated from two anodic and cathodic peaks (see **Figure S8** for calculation details) range between 0.5 and 1.0, suggesting combined capacitive and diffusion-limited charge storage processes. Notably, LiVO showed larger *b*-values in all four redox peaks than NaVO and KVO (**Figure 4b**), suggesting its peak current is more responsive to scan rate and thus a swift charge extraction and insertion process during the electrochemical cycling. The fast charge transport kinetics

revealed in LiVO is congruent with its large interlayer and superior rate and cycling performance. The excellent charge transport behavior of LiVO is also supported by electrochemical impedance spectroscopy (EIS) measurements. Although all AVOs showed similar solution resistances (~ 7 ohms) (**Figure 4c**), LiVO shows the smallest electron charge transfer resistance (~ 70 ohms) compared to NaVO and KVO, indicating its high electronic conductivity at electrode /electrolyte interphase.

Furthermore, we have also conducted galvanostatic intermittent titration technique (GITT) tests of AV_3O_8 at the current density of 0.025 A g^{-1} (**Figure 4d** and **Figure S9**) to study ionic diffusion. The GITT provides thermodynamic hysteresis and kinetic polarization when the overpotential from the quasi-equilibrium states is applied. In each step, the voltage first suddenly drops with a small value due to internal resistance (iR) once the constant current is removed, and then it gradually decreases by the concentration polarization due to the ion

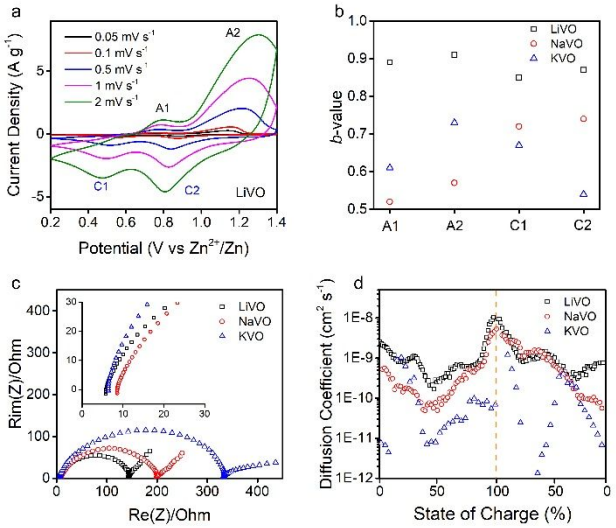

Figure 4. (a) CVs of LiVO at scans rates from 0.05 to 2 mV s^{-1}; (b) *b*-values of AVO (Li^+, Na^+, K^+) indicating surface-controlled (*b*→1.0) and diffusion-limited redox (*b*→0.5) contributions; (c) EIS measurements of AVO at the open circuit voltages; (d) Calculated diffusion coefficient of Zn^{2+}/H^+ in AVO electrodes.

diffusion (η) until reaching the quasi-equilibrium state. LiVO has a small iR drop (~ 0.012 V) and a small value of η, suggesting a large diffusion-coefficient and high electronic conductivity. The diffusion coefficient at each potential during CP testing is calculated based on the following Equation 2:

$$D = \frac{4}{\pi\tau}\left(\frac{n_m V_m}{S}\right)^2\left(\frac{\Delta E_s}{\Delta E_t}\right)^2 \qquad \text{Equation 2}$$

where τ is the duration of the current pulse (s); n_m is the number of moles; V_m is the molar volume of the electrode (cm^3 mol^{-1}); S is the electrode and electrolyte contact area (cm^2); ΔE_s is the steady-state voltage change during the constant current pulse without the iR drop; ΔE_t is the voltage for each current pulse (**Figure S9**). The diffusion coefficient of LiVO with the magnitude between 10^{-8} and 10^{-10} cm^2 s^{-1}, which are certainly higher than those of NaVO and KVO throughout the whole voltage window, and higher than Mn- or V-based Zn-ion cathodes (10^{-12} to 10^{-14} cm^2 s^{-1}). Notably, diffusion coefficients are smaller in the low state of charge (SOC) (< ~ 50%) than those in high SOC (>~ 50%). This could be explained by the formation of $Zn_4(OH)_6SO_4{\cdot}4H_2O$ precipitates during the discharge process (see the following discussion on *in situ* XRD), which is a poor electronic and ionic conductor and impedes the ionic transport at the electrode/electrolyte interface.

The phase evolution of three vanadate materials during the electrochemical cycling was studied using *in situ* synchrotron XRD characterizations. During *in situ* XRD measurements, CV scans were conducted under the voltage window between 0.2 V and 1.4 V (vs. Zn^{2+}/Zn) at a scan rate of 0.5 mV s^{-1} in a 3 M $ZnSO_4$ electrolyte. **Figure S10** shows the complete *in situ* XRD patterns, and their Contour plots are shown in **Figure 5**. **Figure 5a** shows the *in situ* XRD pattern of LiVO, where (110), (111), and (204) diffraction peaks can be indexed. Although all three diffraction peaks underwent similar peak position and intensity evolution, the (204) peak was chosen for the detailed study

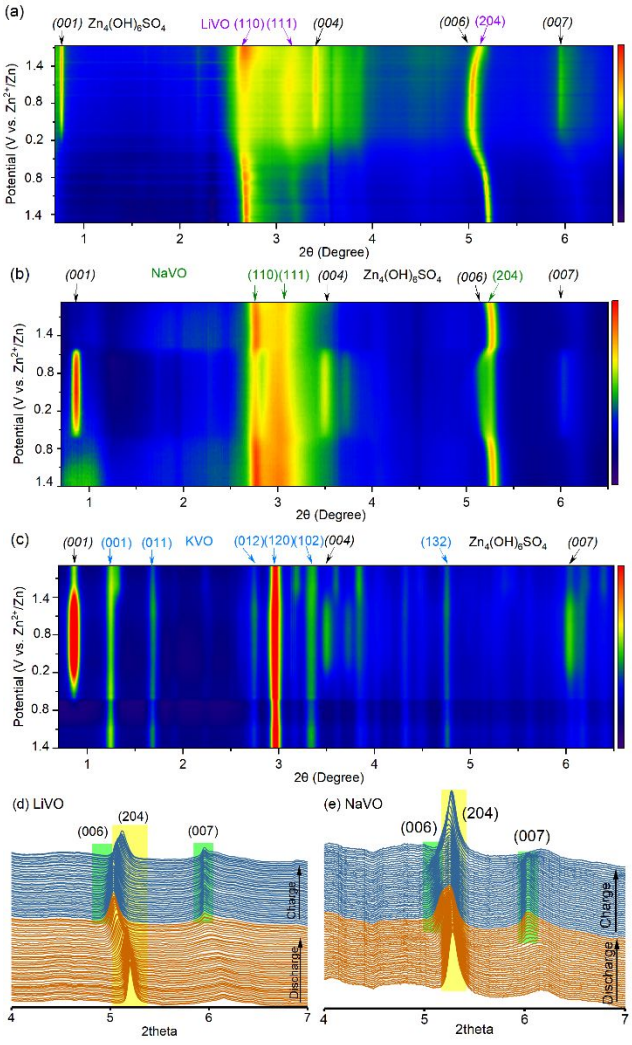

Figure 5. (a/b/c) Contour plot of *in situ* XRD measurements of Li/Na/K; (d/e) The variation of crystal lattices of AVO with zoom-in of (204).

due to its high signal-to-noise ratio and less interference from background scattering (**Figure 5d**). When the voltage decreased

from 1.4 V to 0.2 V (discharging), the (204) peak shifts to a lower 2θ angle from 5.58° to 5.42°, equivalent to the increase of d_{204} from 1.71 Å to 1.76 Å. In the consecutive charging from 0.2 V to 1.4 V, it restored to a higher 2θ angle and a decreased d_{204} value. The reversible changes of d_{204} values suggested the expansion of LiVO lattice upon the insertion of Zn^{2+} (discharging) since reduced vanadium ions have an increased ionic radius, an expanded V-O bond length, and an increased lattice unit compared with the oxidized vanadium ions. Similarly, the lattice of LiVO shrunk upon the extraction of Zn^{2+} (charging).

In addition to the LiVO phase, the Contour plot in **Figure 5a** also shows a layered $Zn_4(OH)_6SO_4$ phase with characteristic basal diffraction planes (00*l*; *l*: 1, 4, 6, and 7) following a quantitative correlation of d_{00l} =11.01 Å/*l*. It is known that the insoluble $Zn_4(OH)_6SO_4$ phase formed upon a non-faradaic reaction between $ZnSO_4$ and OH^-, an indicative of local depletion of H^+. Therefore, $Zn_4(OH)_6SO_4$ has been considered an indirect titration phase for the H^+ intercalation. Namely, the proton insertion caused the decreased concentration of proton nearby the surface of LiVO and resulted in the formation of $Zn_4(OH)_6SO_4$, though the $ZnSO_4$ electrolyte is mildly acidic. Besides demonstrating Zn^{2+} and H^+ dual-ion storage, the evolution of $Zn_4(OH)_6SO_4$ and LiVO phases during the electrochemical cycling, especially (204) peak from LiVO and adjacent (006) and (007) peaks from $Zn_4(OH)_6SO_4$, also reveal sequential intercalation and deintercalation of Zn^{2+}/H^+, highlighted in **Figure 5d**. Specifically, during discharging process from 1.4 V to 0.2 V, the (204) peak of LiVO first shifted to lower 2θ angles, and the $Zn_4(OH)_6SO_4$ phase didn't form, indicating Zn^{2+} intercalation first occurred (note that $Zn_4(OH)_6SO_4$ formation coincided with the proton insertion). As the voltage continuously decreased, the LiVO (204) peak position became unchanged, while (006) and (007) peaks from $Zn_4(OH)_6SO_4$ phase appeared and intensified, indicating H^+ intercalation occurred after Zn^{2+} intercalation. The opposite trends were observed during the charging process. These potentiodynamic changes in LiVO and $Zn_4(OH)_6SO_4$ phases indicated that dual-ion intercalation followed sequences of $Zn^{2+} \rightarrow H^+$ during discharging and $H^+ \rightarrow Zn^{2+}$ during charging.

The Zn-ion storage of NaVO and KVO are also studied with *in situ* XRD tests (**Figure S10** and **Figures 5b** and **5c**). A similar evolution of diffraction peaks from NaVO and KVO vanadate phases and $Zn_4(OH)_6SO_4$ phase were observed, indicating a similar Zn^{2+}/H^+ dual-ion storage. However, there are several distinct differences in diffractions from LiVO, NaVO, and KVO. Firstly, NaVO and KVO show much stronger diffraction peaks than LiVO because NaVO and KVO materials have much-ordered vanadate structures, also evidenced in **Figure 1**. Secondly, compared to LiVO and NaVO, KVO materials show a less distinct shifting of vanadate diffraction peaks, suggesting a sluggish and less significant Zn^{2+} intercalation. This is also congruent with the electrochemical measurements shown in **Figure 3**, where KVO has much inferior storage capacity compared to LiVO and NaVO. Overall, LiVO shows much more reversible and better kinetics of Zn^{2+} and H^+ dual-storage than NaVO and KVO in the aqueous zinc-ion battery.

This study showed that pre-alkalization could significantly modify the local structure of vanadate materials for improved Zn^{2+} and H^+ transport kinetics in Zn-ion batteries. It is notable that pre-alkalization is different from metal ion doping, which is also a commonly used strategy to modify the electrode material.[36, 37] Pre-alkalization allows alkali intercalation in the interlayer region of the layered electrode, often modifying the interlayer distance and thus the transport of charge carriers between metal-oxygen molecular layers. On the other hand, metal ion doping allows the transition metal ions to substitute the host metal ion in the metal-oxygen framework, modifying the electronic structure and electronic conductivity of the host electrode to tailor the charge transfer process.

Conclusions

We have reported a pre-alkalization approach as a versatile toolkit to prepare vanadate cathode materials for aqueous Zn-ion batteries. This scalable approach using recyclable inorganic alkali salt solutions show great promise for preparing disordered vanadium oxide electrode. The resulting vanadium oxide materials with an extensive open framework have superior electrochemical performance in large capacities, excellent rate capabilities, and cycle life. Comprehensive X-ray structural analysis demonstrates that the hydrated alkali metal ions regulate the formation reaction mechanism of AxV_3O_8 materials. Furthermore, we conclude that hydrated Li-ions have the largest hydrated radius and the slowest ion mobility, leading to highly disordered LiVO with considerable interlayer distance and an open V-O framework. Electrochemical measurements show that the LiVO prepared from such an approach exhibits a high specific capacity of 308 mAh g^{-1} at 0.05 A g^{-1} in aqueous Zn-ion batteries and improved electrochemical reaction kinetics with higher ionic conductivity compared to those of the NaVO and KVO cathodes. This new study provides a fundamental understanding of designing layered V_3O_8 materials with the tailored local structure for high-performance battery cathode materials.

Author Contributions

X.S. and X.T. conceived the research idea and designed the experiments. X.S. and F.G. contributed to the material synthesis and characterizations. X.S. contributed to the electrochemical experimental measurements and analysis. X.S., S.K., X.T., M.A., G.K., and D.O. contributed to the *in-situ* X-ray measurements. S.K. and X.S. contributed to the X-ray analysis. X.S. and X.T. wrote the manuscript. X.T. supervised the project. All authors discussed the results and commented on the manuscript.

Conflicts of interest

The authors declare no competing financial interest.

Acknowledgments

This research received financial support from the US Department of Energy (DOE), Office of Science, Basic Energy Sciences under Award DE-SC0018922 (XS, SK). This research used 28-ID-1 beamline of the National Synchrotron Light Source II, a US Department of Energy (DOE) Office of Science User Facility operated for the DOE Office of Science by Brookhaven National Laboratory under Contract No. DE-SC0012704. This material is based upon work supported by the National Science Foundation under Grant No. 2236704 (XT). We acknowledge the technical support from the University Instrument Center at the University of New Hampshire for the EDXS and SEM measurements.

References

1. P. Canepa, G. S. Gautam, D. C. Hannah, R. Malik, M. Liu, K. G. Gallagher, K. A. Persson and G. Ceder, *Chemical Reviews*, 2017, **117**, 4287-4341.
2. J. B. Goodenough and Y. Kim, *Chem. Mat.*, 2010, **22**, 587-603.
3. H. Kim, J. Hong, K.-Y. Park, H. Kim, S.-W. Kim and K. Kang, *Chemical Reviews*, 2014, **114**, 11788-11827.
4. J. Shin, J. Lee, Y. Park and J. W. Choi, *Chemical Science*, 2020, **11**, 2028-2044.
5. B. Tang, L. Shan, S. Liang and J. Zhou, *Energy & Environmental Science*, 2019, **12**, 3288-3304.
6. J. Ding, H. Gao, D. Ji, K. Zhao, S. Wang and F. Cheng, *Journal of Materials Chemistry A*, 2021, **9**, 5258-5275.
7. C. J. Xu, B. H. Li, H. D. Du and F. Y. Kang, *Angewandte Chemie-International Edition*, 2012, **51**, 933-935.
8. H. Pan, Y. Shao, P. Yan, Y. Cheng, K. S. Han, Z. Nie, C. Wang, J. Yang, X. Li, P. Bhattacharya, K. T. Mueller and J. Liu, *Nature Energy*, 2016, **1**, 16039.
9. W. Sun, F. Wang, S. Hou, C. Yang, X. Fan, Z. Ma, T. Gao, F. Han, R. Hu, M. Zhu and C. Wang, *Journal of the American Chemical Society*, 2017, **139**, 9775-9778.
10. F. Wan, L. Zhang, X. Dai, X. Wang, Z. Niu and J. Chen, *Nature Communications*, 2018, **9**, 1656.
11. K. Zhu, T. Wu and K. Huang, *Advanced Energy Materials*, 2019, **9**, 1901968.
12. V. Verma, S. Kumar, W. Manalastas, Jr., J. Zhao, R. Chila, S. Meng, P. Kidkhunthod and M. Srinivasan, *Acs Applied Energy Materials*, 2019, **2**, 8667-8674.
13. C. Xia, J. Guo, Y. Lei, H. Liang, C. Zhao and H. N. Alshareef, *Advanced Materials*, 2018, **30**, 1705580.
14. N. Zhang, F. Y. Cheng, Y. C. Liu, Q. Zhao, K. X. Lei, C. C. Chen, X. S. Liu and J. Chen, *Journal of the American Chemical Society*, 2016, **138**, 12894-12901.
15. H. Y. Shi, Y. J. Ye, K. Liu, Y. Song and X. Q. Sun, *Angewandte Chemie-International Edition*, 2018, **57**, 16359-16363.
16. K. W. Nam, S. S. Park, R. dos Reis, V. P. Dravid, H. Kim, C. A. Mirkin and J. F. Stoddart, *Nature Communications*, 2019, **10**.
17. X. Wu, Y. Xu, C. Zhang, D. P. Leonard, A. Markir, J. Lu and X. Ji, *Journal of the American Chemical Society*, 2019, **141**, 6338-6344.
18. L. Y. Zhang, L. Chen, X. F. Zhou and Z. P. Liu, *Advanced Energy Materials*, 2015, **5**, 1400930.
19. H. Huang, D. Kundu, R. Yan, E. Tervoort, X. Chen, L. Pan, M. Oschatz, M. Antonietti and M. Niederberger, *Advanced Energy Materials*, 2018, **8**, 1802800.
20. V. Soundharrajan, B. Sambandam, S. Kim, M. H. Alfaruqi, D. Y. Putro, J. Jo, S. Kim, V. Mathew, Y.-K. Sun and J. Kim, *Nano Letters*, 2018, **18**, 2402-2410.
21. F. Wan, S. Huang, H. Cao and Z. Niu, *ACS Nano*, 2020, **14**, 6752-6760.
22. J. Yao, Y. Li, R. C. Massé, E. Uchaker and G. Cao, *Energy Storage Materials*, 2018, **11**, 205-259.
23. D. Bin, W. Huo, Y. Yuan, J. Huang, Y. Liu, Y. Zhang, F. Dong, Y. Wang and Y. Xia, *Chem*, 2020, **6**, 968-984.
24. M. Yan, P. He, Y. Chen, S. Wang, Q. Wei, K. Zhao, X. Xu, Q. An, Y. Shuang, Y. Shao, K. T. Mueller, L. Mai, J. Liu and J. Yang, *Advanced Materials*, 2018, **30**, 1703725.
25. K. Zhu, T. Wu and K. Huang, *Advanced Energy Materials*, 2019, **9**, 1901968.
26. X. Shan, S. Kim, A. M. M. Abeykoon, G. Kwon, D. Olds and X. Teng, *Acs Applied Materials & Interfaces*, 2020, **12**, 54627-54636.
27. S. Kim, X. Shan, M. Abeykoon, G. Kwon, D. Olds and X. Teng, *Acs Applied Materials & Interfaces*, 2021, **13**, 25993-26000.
28. Q. Pang, C. Sun, Y. Yu, K. Zhao, Z. Zhang, P. M. Voyles, G. Chen, Y. Wei and X. Wang, *Advanced Energy Materials*, 2018, **8**.
29. X. Rui, Y. Tang, O. I. Malyi, A. Gusak, Y. Zhang, Z. Niu, H. T. Tan, C. Persson, X. Chen, Z. Chen and Q. Yan, *Nano Energy*, 2016, **22**, 583-593.
30. X. Liu, J. Zeng, H. Yang, K. Zhou and D. Pan, *RSC Advances*, 2018, **8**, 4014-4031.
31. S. Suriyakumar, A. Varma, V. Surendran, K. Jasuja and M. M. Shaijumon, *Batteries & Supercaps*, 2022, **5**, e202100243.
32. R. R. Kapaev and K. J. Stevenson, *Journal of Materials Chemistry A*, 2021, **9**, 11771-11777.
33. D. S. Charles, F. Guo, X. Shan, S. Kim, Z. W. Lebens-Higgins, W. Xu, D. Su, L. F. J. Piper and X. Teng, *Journal of Materials Chemistry A*, 2021, **9**, 15629-15636.
34. B. E. Conway, *J. Electrochem. Soc.*, 1991, **138**, 1539-1548.
35. V. Augustyn, J. Come, M. A. Lowe, J. W. Kim, P. L. Taberna, S. H. Tolbert, H. D. Abruna, P. Simon and B. Dunn, *Nat. Mater.*, 2013, **12**, 518-522.
36. M. Chuai, J. Yang, M. Wang, Y. Yuan, Z. Liu, Y. Xu, Y. Yin, J. Sun, X. Zheng, N. Chen and W. Chen, *eScience*, 2021, **1**, 178-185.
37. X. Shan, F. Guo, K. Page, J. C. Neuefeind, B. Ravel, A. M. M. Abeykoon, G. Kwon, D. Olds, D. Su and X. Teng, *Chemistry of Materials*, 2019, **31**, 8774-8786.